RSC Advances

PAPER

View Article Online
View Journal | View Issue

Cite this: *RSC Adv.*, 2025, **15**, 47989

Atomistic investigation of grain boundary strengthening and composition-dependent mechanical properties in CuNi binary alloys

Sanzida Naznin Mim, Zihad Hossain and Md Lokman Ali *

This work examines the influence of grain boundary (GB) and chemical composition on the elastic and mechanical properties of CuNi binary alloys through molecular dynamics simulations. Three configurations, a defect-free single crystal (GB Non) and two symmetric tilt GBs, Σ5 (310) and Σ13 (314), were evaluated across five compositions. The computed elastic constants reveal that C_{11} consistently exceeds C_{12} and C_{44} (C_{11} = 185.03, C_{12} = 124.34, and C_{44} = 88.99 for $Cu_{0.50}Ni_{0.50}$) a characteristic signature of FCC alloys. The introduction of GBs enhances stiffness, indicating a structural strengthening effect attributed to local atomic rearrangements, with the magnitude of enhancement varying by composition. All configurations satisfy the Born–Huang mechanical stability criteria, confirming their elastic stability. Across all compositions, Young's modulus (E) remains the highest among the three moduli, reflecting the alloys pronounced resistance to uniaxial tensile deformation. Stress–strain analysis further highlights the superior performance of GB Σ13, which exhibits the highest peak stress among all configurations, with peak strength increasing progressively with higher Cu content. This correlates with its highest hardness and melting point (1463.43 K) as well as enhanced machinability compared to GB Non and GB Σ5 with highest Cu concentrations. Cauchy pressure, Poisson's ratio, Pugh's ratio, and Frantsevich's criterion consistently classify the alloys as ductile, while direction-dependent properties reveal anisotropic behavior. Furthermore, reversing the Cu/Ni ratio has negligible impact on the elastic response for GB Non and GB Σ5, as observed for $Cu_{0.375}Ni_{0.625}$ and $Cu_{0.625}Ni_{0.375}$. These results provide atomistic insights into the interplay between GB structure, composition, and mechanical performance, offering valuable guidance for optimizing CuNi alloys in structural applications.

Received 26th September 2025
Accepted 28th November 2025

DOI: 10.1039/d5ra07327h

rsc.li/rsc-advances

1. Introduction

Binary alloys, formed by combining two principal metallic elements, represent one of the most fundamental and versatile classes of engineering materials.[1] They frequently surpass their pure counterparts by exhibiting higher strength, hardness, enhanced ductility and corrosion resistance,[2,3] which has established their significance across diverse fields such as aerospace,[4,5] marine[6,7] and biomedical applications.[8] The enhanced performance often arises from mechanisms involve solid solution strengthening, precipitation hardening, and atomic size mismatch, which impedes dislocation motion and improves resistance to mechanical deformation.[9–11] Additionally, the ability to form single-phase solid solutions or intermetallic compounds allows binary alloys to serve as model systems for fundamental studies of lattice distortion, diffusion, and defect interactions.[12,13] Among binary systems, CuNi alloys are particularly noteworthy and most extensively studied[14] due to their unique combination of mechanical strength, ductility, corrosion resistance, and thermal stability. CuNi alloys, originally named cupronickel due to ores that appeared copper-like but actually contained nickel,[15] are highly resistant to seawater corrosion, making it indispensable in marine engineering, heat exchangers, condensers, and chemical processing industries.[16,17] Their nearly complete solid solubility and simple FCC structure provide an ideal platform for studying lattice distortion, diffusion, and defect interactions, while atomistic studies reveal that reduced Cu content lowers defect formation energies and enhances atomic mobility.[18] Moreover, CuNi alloys exhibit composition-dependent magnetic properties, further extending their range of technological applications.[19] In addition to structural applications, related Cu–Ni–Zn alloys, referred as nickel silver or German silver, are widely used for decorative purposes due to their silvery appearance and corrosion resistance.[15] This rare combination of technological applicability and scientific tractability has established CuNi alloys as benchmark systems for both experimental and computational investigations.

Recent advances in molecular dynamics (MD) simulations have accelerated understanding of binary alloys by illuminating atomic-scale mechanisms. In case of CuNi alloys, MD studies have revealed composition-dependent stacking fault energies and hetero-deformation mechanisms in gradient nanograined structures,[20,21] as well as the mechanical behavior of nanopillars under

Department of Physics, Pabna University of Science and Technology, Pabna 6600, Bangladesh. E-mail: lokman.cu12@gmail.com

varying loading conditions.[22] First-principles studies have also provided insight into phase stability and structural evolution in Cu–Ni, Cu–Pd, and Ni–Pd binary systems.[23] Grain boundary effects have been explored through atom probe studies, revealing segregation behavior and phase boundaries within the miscibility gap of CuNi thin films.[24] Complementary studies have examined grain boundary segregation structures and their influence on grain size optimization and strengthening mechanisms in nanocrystalline CuNi,[25] while surface segregation phenomena have provided additional understanding of microstructural evolution and interface behavior, aiding the broader understanding of alloy composition and dislocation interactions.[26] Beyond CuNi, Mo-based alloys have been shown to exhibit high-temperature strength and ductility.[27] Other binary alloy systems have also been investigated across a range of compositions and properties For example, NiCr alloys produced *via* conventional powder metallurgy were studied in detail for their microstructural and mechanical behavior.[28] Grain boundary effects in binary alloys have gained significant attention, with L'vov *et al.*[29] analyzing the influence of grain boundaries on the distribution of alloying elements, and Gibson *et al.*[30] exploring how segregation-induced changes in grain boundary cohesion can lead to embrittlement. Foundational theoretical and computational work, such as Hillert and Sundman's study on solute drag effects on grain boundary motion,[31] providing a deeper understanding of diffusion and interface phenomena in binary alloys.

This work utilizes molecular dynamics (MD) simulations to investigate the influence of alloy composition and grain boundaries on the mechanical behavior of the CuNi binary alloy. Two different types of grain boundaries were considered, and five CuNi compositions were systematically studied. The embedded-atom method (EAM) potential was employed to calculate elastic constants and a range of mechanical properties, including Pugh's ratio, Poisson's ratio, Cauchy pressure, and the machinability index. Additionally, hardness, melting point, and direction-dependent properties were examined. Our results indicate that grain boundary Σ13 has a significant influence on the investigated properties. The machinability index was found to be higher for GB Σ13 compared to all other states. All properties showed clear composition dependence in GB Σ13, whereas in Non-GB and GB Σ5 states the elastic response remained nearly unchanged upon reversing the Cu and Ni ratio, as observed for $Cu_{0.375}Ni_{0.625}$ and $Cu_{0.625}Ni_{0.375}$. Furthermore, elastic anisotropy was evaluated to understand directional dependence of mechanical response. Finally, stress–strain curves were analyzed to provide deeper insight into the deformation mechanisms, revealing the interplay between composition, grain boundary character, and mechanical performance of CuNi alloys.

2. Computational methods and models

2.1 Interatomic potential

The Embedded-Atom Method (EAM)[32–35] is a semi-empirical potential model specifically designed for simulation of metallic systems. Originating from the principles of Density Functional Theory (DFT),[36] it offers a robust and reliable means of analyzing atomic interactions in metals. EAM has been widely employed to study surface properties, nanoparticle behavior, phase changes, solidification, and defect evolution. Because of its effectiveness in capturing metallic bonding characteristics, it is sometimes referred to as the glue potential[37] and remains a key tool in computational materials science. This research employs the EAM potential for the CuNi binary alloy, as developed by Fischer *et al.*, to achieve more accurate modeling of atomic interactions.[38] A key advantage of EAM over simple pair potentials lies in its treatment of many-body effects. Instead of relying solely on pairwise forces, EAM integrates an embedding energy term that depends on the local electron density from neighboring atoms.[33] This density reflects the collective influence of surrounding atoms, allowing the method to represent metallic bonding, alloy interactions, and surface phenomena with greater accuracy. Despite it accounts for complex atomic behavior, EAM is efficient and well-suited for large atomistic studies. In its standard formulation,[32,39] the total energy of a monatomic system is expressed as:

$$E_{\text{tot}} = \frac{1}{2}\sum_{ij} V(r_{ij}) + \left(\sum_{i} F(\rho_i)\right)$$

In this formalism, $V(r_{ij})$ denotes the pairwise interaction potential between atoms i and j, which depends on the separation distance r_{ij}. The term $F(\rho_i)$ represents the embedding energy, determined by the local electron density ρ_i at atom i. The local electron density is obtained from the sum of contributions of neighboring atoms,

$$\rho_i = \sum_{j \neq i} \rho(r_{ij})$$

where $\rho(r_{ij})$ describes the electron density influence from atom j at distance r_{ij}. The total embedding energy, $\sum_i F(\rho_i)$, captures essential volume-dependent many-body effects that go beyond simple pairwise interactions. These effects are critical for accurately describing metallic bonding, structural stability, and defect behavior. By combining physical realism with computational efficiency, the EAM method has become a key tool for simulating mechanical properties, defect evolution, and phase transformations in metallic systems over a wide range of length scales.

2.2 Molecular dynamics simulations

To investigate the atomic-scale behavior and mechanical response of the selected CuNi binary alloy, Molecular Dynamics (MD) simulations were conducted using the Large-scale Atomic/Molecular Massively Parallel Simulator (LAMMPS) package.[40] This software was chosen for its strong capability to model large-scale atomic systems and its extensive validation for metallic materials. The alloy was selected based on the availability of a reliable interatomic potential capable of accurately representing its structural stability, defect behavior, and mechanical characteristics. Interatomic forces were described using the Embedded Atom Method (EAM),[32] a semi-empirical

potential specifically developed for metallic systems. The EAM formalism accounts for many-body interactions through an embedding energy term that depends on the local electron density, enabling more realistic modeling compared to simple pair potentials. This potential type has been widely employed in simulations addressing dislocation dynamics, grain boundary (GB) interactions, and lattice distortion effects.

The initial atomic configurations were generated using ATOMSK[41] to construct simulation cells with and without grain boundaries. The GB-containing models were relaxed *via* conjugate gradient minimization in LAMMPS to remove residual stresses and achieve energetically stable configurations prior to loading. All simulations were performed under Periodic Boundary Conditions (PBC) in three dimensions, creating an effectively infinite lattice and minimizing surface effects. This approach allows atoms at one boundary of the simulation cell to interact seamlessly with their periodic images, ensuring a bulk-like environment. Within the MD framework, atoms were initially distributed in a face-centered cubic (FCC) lattice arrangement corresponding to the equilibrium structure of the binary alloy. The simulations were performed in a quasi-static regime at 0 K using energy minimization. This setup ensured thermodynamic equilibrium and maintained the desired simulation conditions. The resulting trajectories were subsequently analyzed to extract structural, elastic, and defect-related properties, focusing on how lattice distortion, GB structure, and dislocation interactions influence the alloy's mechanical behavior. To further ensure reproducibility and clarity of the computational setup, all simulation parameters explicitly defined in the LAMMPS input scripts have been described in this work properly. The simulations were performed using the metal unit system with fully periodic boundary conditions. The interatomic interactions were modeled using the EAM/alloy potential. Energy minimization employed stringent convergence criteria an energy tolerance of 0.0, a force tolerance of 1.0×10^{-3}, and limits of 1×10^{7} iterations and 1×10^{7} force evaluations, ensuring well-relaxed and mechanically stable configurations prior to analysis. The integration time step for all simulations was set to 1.0 fs, providing accurate and stable numerical integration of atomic trajectories. Grain-boundary relaxation was conducted using the fix box/relax aniso 0.0 command, consistent with the procedures defined in the input files. A small random atomic displacement of 1×10^{-5} Å was additionally applied to avoid metastable energy traps during relaxation.

2.3 Random and grain boundary models constructions

In this study, nanocrystalline bicrystal models containing three grain boundary configurations, a defect-free single crystal (GB Non), Σ5 (310), and Σ13 (314) symmetric tilt grain boundaries, were constructed using the molecular dynamics-based modeling tool ATOMSK.[41] These GB types were selected due to their prevalence in FCC metals and their distinct misorientation angles, enabling systematic evaluation of interfacial effects on mechanical properties. Specifically, GB Σ5 (310) and GB Σ13 (314) represent two structurally distinct and widely studied GBs in FCC systems.[42–44] GB Σ5 is a high energy boundary with larger local free volume, making it more susceptible to early defect nucleation and GB Σ13 is a lower energy and more coherent boundary that strongly resists dislocation transmission. This contrast provides a meaningful basis for studying how GB structure and energy influence deformation behavior in CuNi alloys. Each GB model was generated for five distinct CuNi binary alloy compositions, enabling a systematic comparison of elastic behavior across varying chemical ratios. The bicrystal orientation for the GB Σ5 model was set along [310], [−130], and [001], while the GB Σ13 model was oriented along [314], [5−72], and [111]. For the defect-free single crystal (GB Non), the orientation was taken as [100], [010], and [001] along the x, y, and z axes, with a supercell volume of approximately $9.504 \times 9.504 \times 9.504$ nm^3 and containing around 78 732 atoms. The GB Σ5 (310) model contains 60 144 atoms, with a supercell volume of $12.68 \times 4.224 \times 4.93$ nm^3. Finally, the Σ13 (314) GB model contains 66 960 atoms with a supercell volume of $6.34 \times 2.112 \times 2.82$ nm^3. The pure Ni supercells were chemically randomized *via* substitution with the desired Cu fraction to achieve uniform solid solutions in each composition. Atomic-scale structures were visualized with the Open Visualization Tool (OVITO),[45,46] and defect characterization was performed using Common Neighbor Analysis (CNA).[47] Representative atomic configurations for GB Non, GB Σ5, and GB Σ13, in three compositions are presented in Fig. 1, confirming the FCC lattice structure in each case.

2.4 Computation of elastic stiffness constants and mechanical properties

The elastic constants of the CuNi binary alloy models were evaluated using the small-strain deformation method implemented in LAMMPS, which determines stiffness by applying infinitesimal strains and measuring the resulting stress response. Six independent Voigt deformation modes were applied in both positive and negative directions, with a strain magnitude of $\pm 1 \times 10^{-5}$ to ensure the linear elastic regime was preserved. All calculations were conducted at 0 K under static conditions, without thermal ensembles, to eliminate temperature-induced noise and improve accuracy. This approach is commonly used to isolate intrinsic elastic and defect-controlled deformation behavior. While finite-temperature effects may influence dislocation mobility and GB-mediated mechanisms, the comparative trends among compositions and grain-boundary types remain physically meaningful. Prior to each deformation step, a small random displacement of 1×10^{-5} Å was introduced to all atoms to avoid the system becoming trapped in saddle points of the energy landscape. After each strain was applied, energy minimization was performed using the conjugate gradient method with strict convergence criteria, energy tolerance, "etol = 0.0", force tolerance, "ftol = 1×10^{-3}", and maximum iterations, "maxiter = 1×10^{7}". The simulation box was relaxed anisotropically using the "fix box/relax aniso 0.0" command to allow for stress equilibration in all directions. The components of the stress tensor (pxx, pyy, pzz, pxy, pxz, pyz) were recorded both before

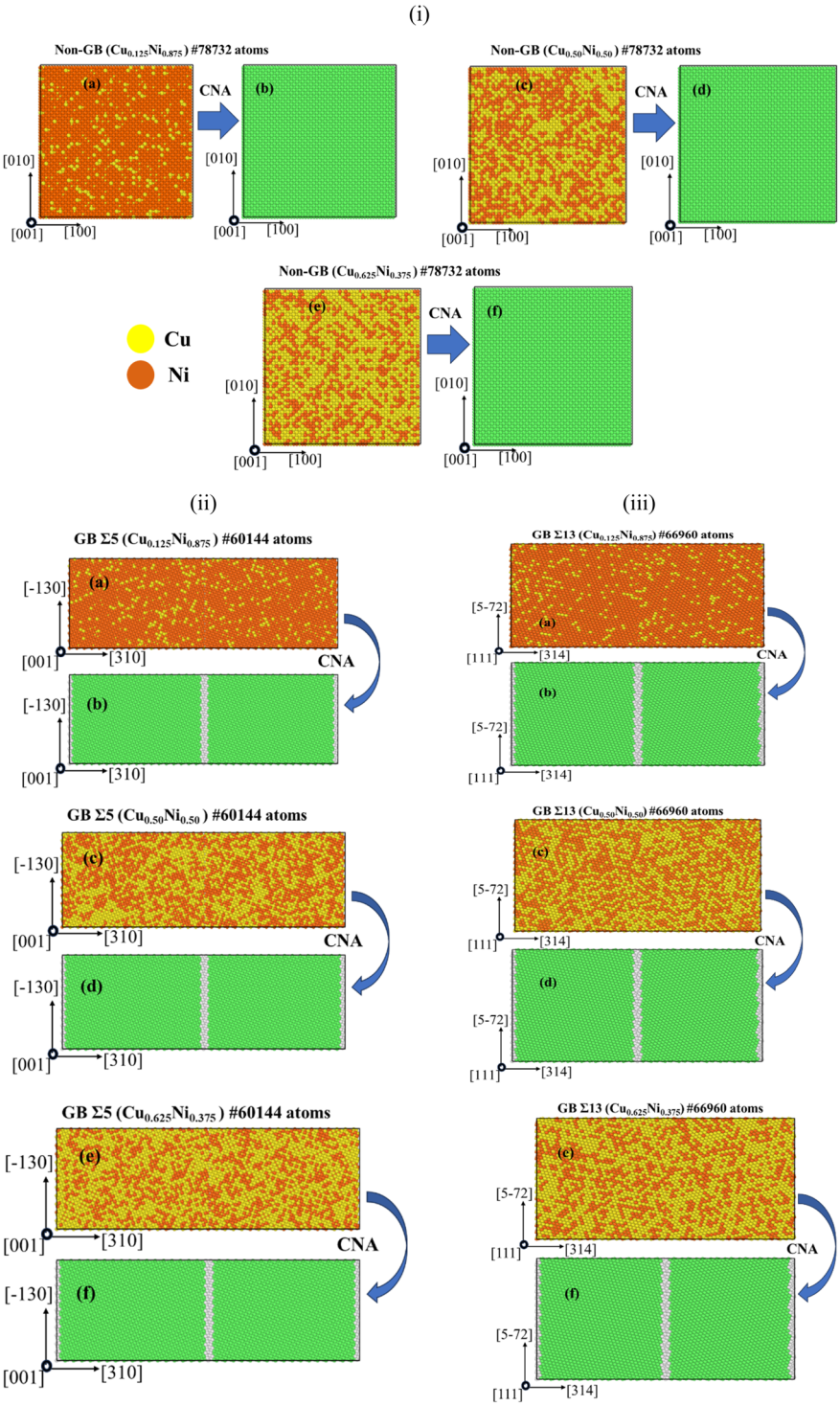

Fig. 1 Atomic configurations and structural evolution of CuNi binary alloy, showing (a) $Cu_{0.125}Ni_{0.875}$, (c) $Cu_{0.50}Ni_{0.50}$, and (e) $Cu_{0.625}Ni_{0.375}$ for (i) Non-GB, (ii) GB Σ5 (310), and (iii) GB Σ13 (314). The corresponding color maps in (b), (d) and (f) represent common neighbor analysis (CNA) for atomic arrangements.

and after deformation. Stress differences were used to construct the full elastic stiffness tensor through finite-difference analysis. A conversion factor, "cfac = 1.0×10^{-4}" was applied to express all elastic constants in gigapascals (GPa). Interatomic forces were modeled using the EAM/alloy potential, chosen for its reliability in describing metallic bonding in multi-component alloys. For each grain boundary configuration, multiple independent simulations were performed to ensure reproducibility. The derived bulk modulus (B), shear modulus (G), and Poisson's ratio (ν) were calculated from the elastic constants using the Voigt–Reuss–Hill (VRH) averaging

scheme.[48–50] These values form the basis for subsequent mechanical property analysis in this study.

3. Results and discussion

3.1 Alloy composition and effects of GB on elastic constants

Elastic constant plays a significant role in defining the bonding characteristics and mechanical properties of solids. By establishing a link between phonon spectrum and Debye temperature, these constants offer crucial insight into mechanical stability and also influence structural integrity as well as the performance of the crystal. They bridge the dynamical and mechanical response of a solid and explains how much deformation the solid can undergo under applied stress and how effectively it regains its original form once the stress is removed. To explain this behaviour explicitly, cubic system requires three independent elastic constants namely, C_{11}, C_{12} and C_{44}. Specifically, C_{11} represents the resistance to longitudinal strain, particularly along [100] direction, while C_{12} and C_{44} denote shear elasticity, reflecting material's resistance to shear and shape changes under transverse strain.[51] The variation of these constants for different alloy compositions were analyzed to examine the effect of grain boundaries on the mechanical stiffness of the system and listed in Table 1. Born stability criteria are employed to ensure the mechanical stability of the studied material. For cubic system these criteria are,[52]

$$C_{11} > 0,\ C_{44} > 0,\ C_{11} + 2C_{12} > 0 \text{ and } C_{11} - C_{12} > 0$$

According to the calculated elastic constants, the all compositions of $Cu_xNi_{(1-x)}$. Binary alloy are mechanically stable, satisfying the extensively predictable Born stability condition.

As illustrated in Fig. 2, the elastic constants are computed for several compositions both with and without the presence of symmetric tilt grain boundaries. In all cases, C_{11} consistently exhibits the highest value, followed by C_{12} and C_{44}, reflecting the typical mechanical behavior of FCC-based alloys. For the $Cu_{0.50}Ni_{0.50}$ composition, the calculated elastic constants show good agreement with previously reported DFT based values,[53] with only moderate deviations attributable to methodological differences. Interestingly, the introduction of grain boundaries results in a noticeable increase in the elastic constants across most compositions. This enhancement suggests that GBs contribute to a structural stiffening effect, likely due to local atomic rearrangements that hinder deformation under applied stress.

Among the three constants, the increase in C_{44} which is associated with shear resistance, is particularly prominent, indicating that GBs may act as barriers to dislocation motion or lattice shearing. Again, GB Σ13 model increases the elastic constants than all other configurations, enhanced stiffness and mechanical stability. This is because atomic arrangement at the GB Σ13 interface may lead to stronger interatomic bonding, which resists deformation more effectively. Additionally, the orientation and character of the symmetric tilt grain boundary in Σ13 introduces less lattice distortion and lower energy mismatch, thereby enhancing the mechanical response. This behavior can be explained by the atomistic structure of the Σ13 symmetric tilt boundary. Unlike Σ5, the Σ13 exhibits a more periodic and well ordered atomic arrangement. This reduces the density of excess free volume and minimizes local structural disorder. Because of this smoother and more organized structure, GB Σ13 has lower energy and allows stress to pass across it more evenly. At the atomic level, the GB Σ13 interface acts as a stronger obstacle to dislocations. The lower distortion helps it

Table 1 The elastic constants C_{ij} (in GPa) of $Cu_xNi_{(1-x)}$ binary alloy

Grain boundary	Alloy composition $Cu_xNi_{(1-x)}$	C_{11}	C_{12}	C_{44}
Non GB	$Cu_{0.125}Ni_{0.875}$	170.37	122.35	78.12
	$Cu_{0.25}Ni_{0.75}$	172.61	122.25	80.62
	$Cu_{0.375}Ni_{0.625}$	195.64	127.66	95.51
	$Cu_{0.50}Ni_{0.50}$	185.03	124.34	88.99
	$Cu_{0.625}Ni_{0.375}$	195.56	127.80	95.44
GB 5	$Cu_{0.125}Ni_{0.875}$	179.68	112.93	78.01
	$Cu_{0.25}Ni_{0.75}$	181.24	113.42	80.62
	$Cu_{0.375}Ni_{0.625}$	204.84	115.95	95.67
	$Cu_{0.50}Ni_{0.50}$	193.76	113.92	88.82
	$Cu_{0.625}Ni_{0.375}$	204.95	115.87	95.29
GB 13	$Cu_{0.125}Ni_{0.875}$	218.53	107.05	37.74
	$Cu_{0.25}Ni_{0.75}$	221.72	106.35	39.56
	$Cu_{0.375}Ni_{0.625}$	227.35	105.96	42.45
	$Cu_{0.50}Ni_{0.50}$	235.06	106.91	46.4
	$Cu_{0.625}Ni_{0.375}$	246.54	109.05	50.48

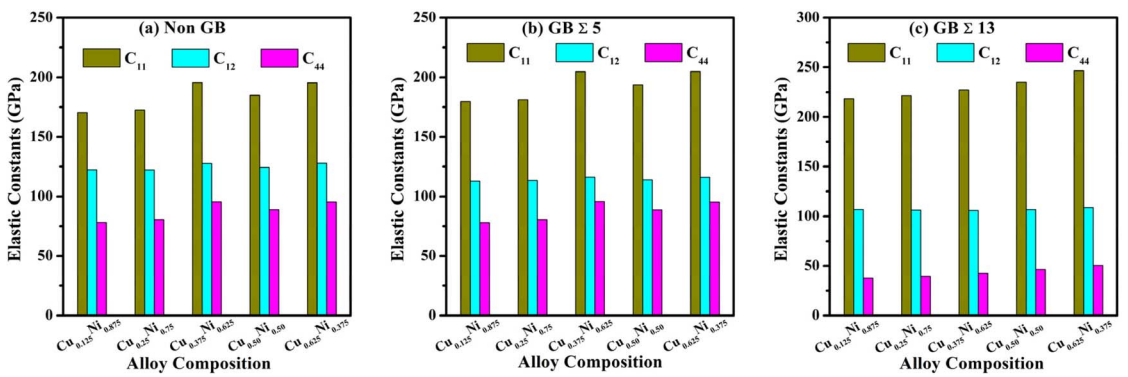

Fig. 2 Influence of alloy composition and grain boundary on the elastic constant (a) Non-GB, (b) GB Σ5 and, (c) GB Σ13 of CuNi binary alloy.

absorb the part of the incoming dislocations and slows down their movement consequently increases the local strengthening. Altogether, the reduced free volume, better atomic alignment, and stronger resistance to dislocation motion make the Σ13 boundary more effective in increasing the elastic constants and overall mechanical stiffness of the alloy. Furthermore, a notable observation is seen when comparing the binary alloys $Cu_{0.375}Ni_{0.625}$ and $Cu_{0.625}Ni_{0.375}$ under both Non GB and GB Σ5 conditions. Although the Cu and Ni concentrations are reversed, their elastic constants are nearly the same. It implies the presence of symmetric or compensating atomic interactions, meaning that swapping Cu and Ni does not drastically change the local bonding environment in the FCC lattice.

3.2 Alloy composition and effects of the GB on mechanical properties

Mechanical behaviour primarily described by three elastic moduli, Young's modulus (E), bulk modulus (B) and shear modulus (G) determined utilizing the elastic constants. In this study, Voigt–Reuss–Hill approximations are employed to calculate this moduli and Poisson's ratio. The Voigt[48] and Reuss[49] models are used to calculate the upper and lower bounds for B and G, respectively, and Hill's approach[50] to determine realistic values by averaging them. Fig. 3 presents the elastic moduli for various alloy compositions under GB conditions. Across all compositions, E consistently appears highest among the three moduli. This reflects the system has relatively high resistance to uniaxial tensile deformation. The Bulk modulus exhibit the second highest with moderate compressibility, while G is notably lowest, indicating limited shear resistance, characteristics of FCC-based systems. Under GB Σ5, all moduli are higher in every composition compared to the other two conditions. This indicates GB Σ5 contribute more strongly to the mechanical strengthening due to favorable atomic structure at the GB interface. Further, $Cu_{0.625}Ni_{0.375}$ shows highest values for E, B, G, suggesting the higher Cu content improves stiffness and resistance to volume changes. However, earlier observations that reversing Cu and Ni ratios does not significantly affect elastic behavior is also evident in this section, as $Cu_{0.375}Ni_{0.625}$ and $Cu_{0.625}Ni_{0.375}$, exhibit very similar E, B, G values. This finding points to mechanical symmetry in this binary system. For validation, the Young's modulus obtained from MD for the equiatomic $Cu_{0.50}Ni_{0.50}$

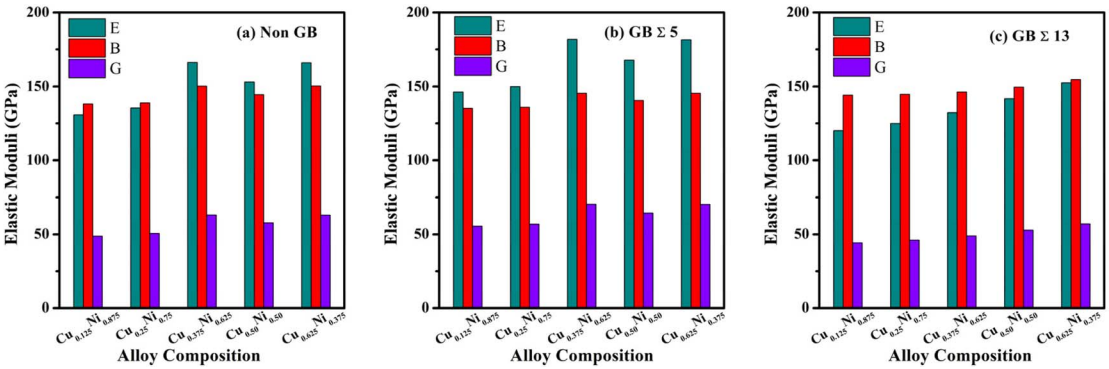

Fig. 3 Influence of alloy composition and grain boundary on the elastic moduli (E, B, G) (a) Non-GB, (b) GB Σ5 and, (c) GB Σ13 of CuNi binary alloy.

Table 2 The calculated values of bulk modulus B (GPa), shear modulus G (GPa), Young's modulus E (GPa), Pugh's ratio B/G, Poisson's ratio ν, Cauchy's pressure ($C_{11}-C_{12}$) of $Cu_xNi_{(1-x)}$ binary alloy

Grain boundary	Grain boundary	B	G	E	B/G	ν	$C_{11}-C_{12}$	ζ	μ_M
Non GB	$Cu_{0.125}Ni_{0.875}$	138.36	48.78	130.95	2.84	0.342	44.23	0.800	1.77
	$Cu_{0.25}Ni_{0.75}$	139.04	50.66	135.51	2.74	0.338	41.63	0.792	1.72
	$Cu_{0.375}Ni_{0.625}$	150.32	63.15	166.18	2.38	0.316	32.15	0.749	1.57
	$Cu_{0.50}Ni_{0.50}$	144.57	57.86	153.15	2.50	0.323	35.35	0.764	1.62
	$Cu_{0.625}Ni_{0.375}$	150.39	63.04	165.94	2.39	0.316	32.36	0.750	1.58
GB 5	$Cu_{0.125}Ni_{0.875}$	135.18	55.49	146.43	2.44	0.319	34.92	0.730	1.73
	$Cu_{0.25}Ni_{0.75}$	136.03	56.96	149.95	2.39	0.316	32.80	0.728	1.69
	$Cu_{0.375}Ni_{0.625}$	145.58	70.33	181.73	2.07	0.292	20.28	0.680	1.52
	$Cu_{0.50}Ni_{0.50}$	140.53	64.44	167.68	2.18	0.301	25.10	0.698	1.58
	$Cu_{0.625}Ni_{0.375}$	145.56	70.22	181.49	2.07	0.292	20.58	0.679	1.53
GB 13	$Cu_{0.125}Ni_{0.875}$	144.21	44.14	120.16	3.27	0.361	69.31	0.616	3.82
	$Cu_{0.25}Ni_{0.75}$	144.81	46.03	124.86	3.15	0.356	66.79	0.608	3.66
	$Cu_{0.375}Ni_{0.625}$	146.42	49.00	132.25	2.99	0.349	63.51	0.596	3.45
	$Cu_{0.50}Ni_{0.50}$	149.63	52.81	141.76	2.83	0.342	60.51	0.586	3.22
	$Cu_{0.625}Ni_{0.375}$	154.88	57.13	152.63	2.71	0.336	58.57	0.576	3.07

alloy ($E = 153.15$ GPa) was compared with literature data. This value falls close to the range of experimentally reported stiffness for CuNi alloys ($E = 163$ for $Cu_{0.46}Ni_{0.54}$ and $E = 172$ for $Cu_{0.55}Ni_{0.45}$)[53–55] and shows reasonable agreement with high-accuracy DFT calculations ($E \approx 171.7$ GPa).[53] Thus, the predicted elastic response is consistent with established references, confirming the reliability of the employed EAM potential. Detailed numeric values are summarized in Table 2.

Poisson's ratio is also obtained using VRH approximations,[50] which along with Pugh's ratio and Cauchy's pressure, helps to evaluate the ductile and brittle nature of a material. Fig. 4 represents bar diagram illustrating both Pugh's and Poisson's ratio for the studied compound $Cu_xNi_{(1-x)}$. The red dashed line in each figure indicates the brittle–ductile transition threshold. The region below this line indicates brittle and above ductile. For Pugh's ratio, values greater than 1.75 indicate ductile behavior, while values below 1.75 indicate brittleness.[54] In contrast, for Poisson's ratio, values above 0.26 are associated with ductility, and those below 0.26 with brittleness.[55] All alloy compositions studied here, under both GB and Non GB conditions, exhibit ductile behavior, as their values lie above the respective thresholds. This ductility is critical for ensuring good machinability of the material. Notably, the introduction of GB Σ13 leads to a significant increase in both ratios, enhancing ductility. In contrast, the GB Σ5 model reduces these values, shifting them closer to the brittle region and indicating increased hardness. Furthermore, increasing Cu content gradually shifts the ratios toward the brittle threshold, suggesting that Cu enrichment in this configuration may further harden the alloy.

Cauchy's pressure, defined as the difference between C_{12} and C_{44}, is shown in Fig. 5(a), illustrating the impact of alloy composition and grain boundaries. A positive value of Cauchy's pressure indicates ductility, while a negative value signifies brittleness;[56] hence, the transition line is set at 0 GPa. According to the graph, the trends are consistent with those observed in

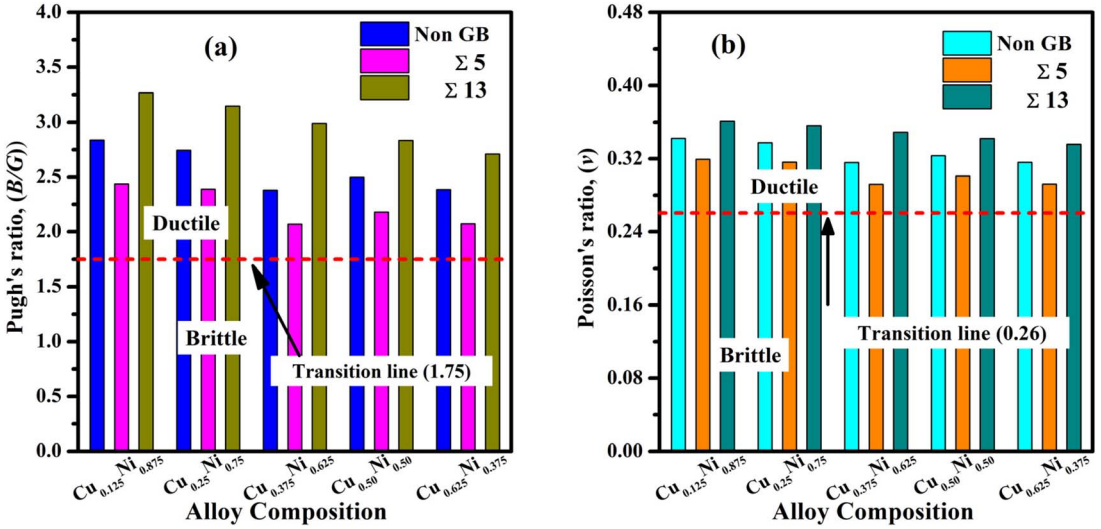

Fig. 4 Influence of alloy composition and grain boundary on (a) Pugh's ratio, and (b) Poisson's ratio of CuNi binary alloy.

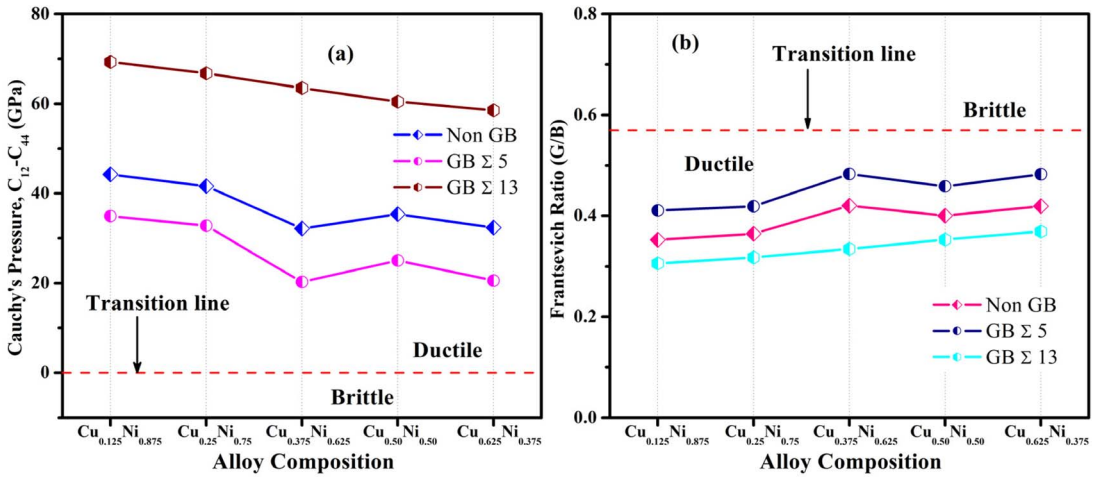

Fig. 5 Influence of alloy composition and grain boundary on the (a) Cauchy's pressure and (b) Frantsevich ratio of CuNi binary alloy.

Pugh's ratio and Poisson's ratio. All configurations of the CuNi binary alloy lie in the ductile region, with GB Σ13 showing enhanced ductility. However, increasing the Cu content reduces ductility which limits toughness and not suitable for devices application,[57] but it can provide advantages in improved hardness, wear resistance, and dimensional stability in specific applications. Similarly, Fig. 5(b) presents the Frantsevich ratio (G/B),[58] another mechanical indicator of ductile–brittle behavior. The critical transition value for this ratio is 0.57, where values below this threshold denote ductility and values above indicate brittleness. All studied CuNi configurations, including those with and without grain boundaries, display G/B values well below the critical line, confirming their ductile nature. Notably, the GB Σ13 configuration exhibits the lowest G/B ratio, reinforcing its superior ductility, whereas higher Cu content generally results in a slight increase in G/B, suggesting a gradual shift toward reduced plasticity.

The machinability index μ_M is defined as the ratio of the bulk modulus to C_{44}, and it reflects how easily a material can be cut, shaped, or machined into various forms for device fabrication. Fig. 6(a) illustrates the grain boundary-dependent variation of μ_M for different compositions of the CuNi binary alloy. The results indicate that increasing Cu concentration within a Ni-supercell leads to a decrease in machinability. However, the introduction of grain boundaries produces the opposite trend. Although GB Σ5 slightly reduces machinability compared to the Non-GB structure, the GB Σ13 model shows a significant increase in machinability. Remarkably, GB Σ13 raises the μ_M value above that of aluminum, a widely known soft metal with $\mu_M = 2.6$.[59] In contrast, diamond, recognized as the hardest known material, exhibits a low machinability index of $\mu_M = 0.8$.[59]

Fig. 6(b) illustrates a dimensionless quantity known as the Kleinman parameter, denoted by ξ, which typically ranges between 0 and 1. This parameter characterizes a material's tendency toward bond bending or bond stretching. A value close to 0 suggests that bond bending is more dominant, while a value near 1 indicates that bond stretching plays a more significant role. The Kleinman parameter is primarily used to evaluate a material's response to tensile and flexural stresses. According to the graph in Fig. 6(b), both the grain boundary structure and the Cu content in the CuNi alloy influence the Kleinman parameter. An overall decrease in ξ is observed with increasing Cu concentration and the introduction of grain boundaries. This decrease suggests that bond bending becomes more dominant, implying a reduction in the material's resistance to deformation under applied stress.

Fig. 6(c) presents the variation of Lame's coefficient (λ) for the CuNi alloy as a function of alloy composition and grain boundary configuration. Lame's coefficient quantifies

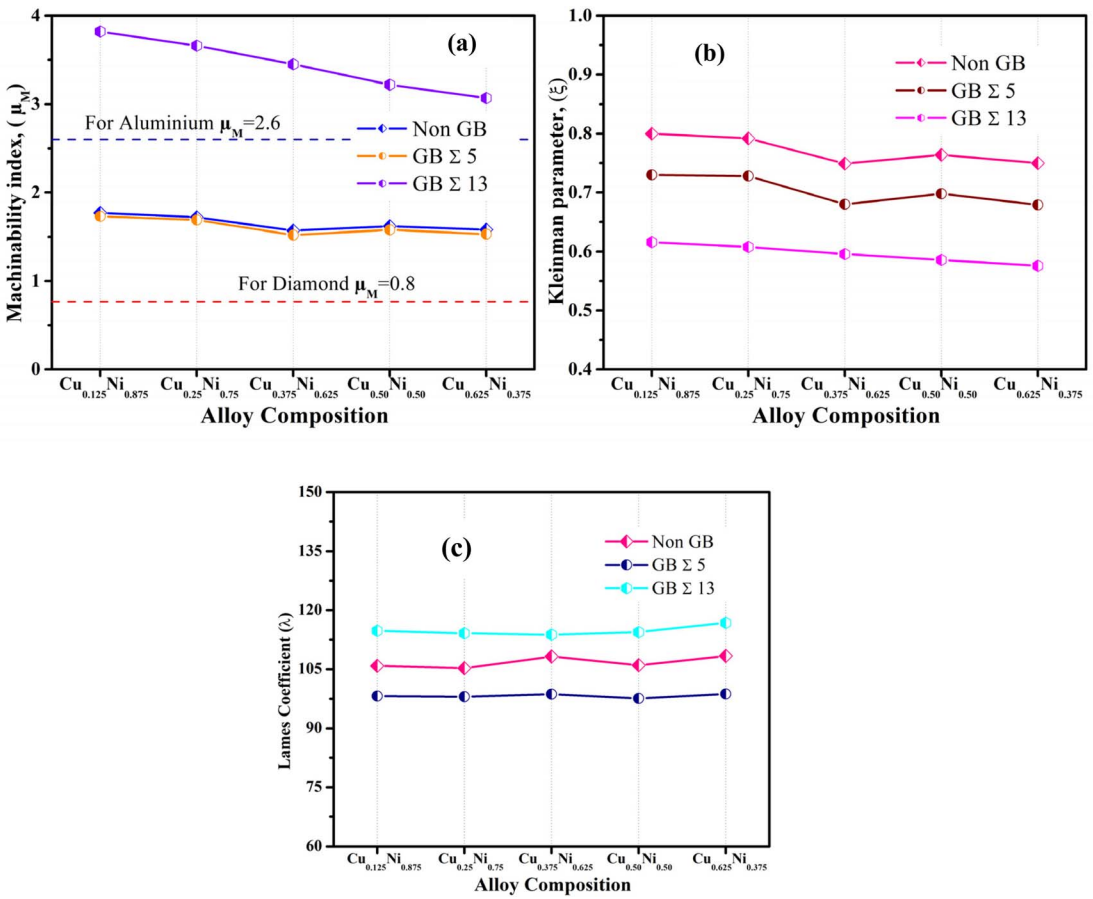

Fig. 6 Influence of alloy composition and grain boundary on (a) machinability index, and (b) Kleinman parameter and (c) Lame's coefficient of CuNi binary alloy.

a material's resistance to uniform compression and is directly related to its bulk elastic response. Higher λ values correspond to greater resistance to volume change under hydrostatic pressure. As shown in the graph, GB Σ13 consistently exhibits the highest λ across all compositions, followed by GB Σ5 and the Non-GB structure. The relatively stable trend of λ with varying Cu content indicates that the alloy maintains a nearly constant volumetric stiffness despite compositional changes. The elevated λ values for GB Σ13 suggest improved resistance to isotropic deformation, which could be beneficial for applications requiring dimensional stability under compressive loads.

3.3 Effect of GB on hardness values

Hardness is a critical mechanical property that determines a material's resistance to localized plastic deformation or indentation and is intrinsically linked to strength, toughness, and wear resistance. In cubic crystal structures such as CuNi alloys, grain boundaries play a vital role in controlling hardness by acting as barriers to dislocation movement. Fig. 7 shows and Table 3 presents the calculated hardness components (H_1–H_8) for various alloy compositions, comparing Non-GB structures with GB Σ5 and GB Σ13 configurations. The hardness values (H_1–H_8) of the CuNi binary alloy are obtained using a theoretical model proposed by Chen *et al.*,[60] along with semi-empirical relations for hardness prediction.[61]

Across all alloy compositions, the introduction of GBs leads to a clear increase in hardness compared to the Non-GB models. Among the two GB types, GB Σ13 shows the highest hardness values, especially in H_1, where the improvement over Non-GB structures are most significant. This indicates that high-angle boundaries like GB Σ13 are more effective at blocking dislocation motion, thereby increasing the material's resistance to indentation.[62] The results also show that the effect of GBs is not uniform across all hardness components, reflecting anisotropic strengthening. In other components except H_1, GB Σ5 also demonstrates a noticeable increase in hardness compared to the Non-GB case, confirming that even lower-angle boundaries can significantly improve strength depending on the deformation mode.

Regarding alloy composition, increasing the Cu content generally leads to higher hardness. An interesting observation is that, for both Non-GB and GB Σ5 structures, interchanging the Cu and Ni concentrations results in nearly identical hardness values. This suggests that, in these cases, hardness is influenced more by the overall alloying effect than by which element is dominant.[62] In contrast, GB Σ13 shows greater sensitivity to composition changes, with certain intermediate CuNi ratios

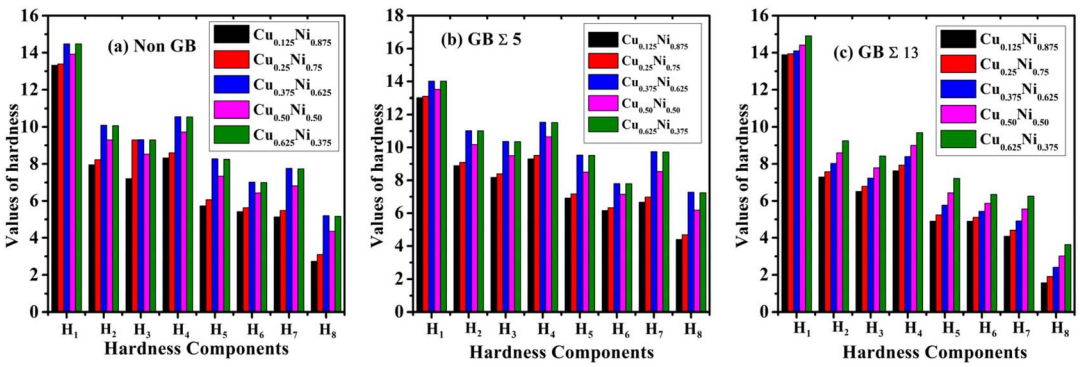

Fig. 7 Influence of alloy composition and grain boundary on hardness (a) Non-GB, (b) GB Σ5 and (c) GB Σ13 of CuNi binary alloy.

Table 3 Influence of grain boundary on the hardness of $Cu_xNi_{(1-x)}$ binary alloy

Grain boundary	Grain boundary (GB)	H_1	H_2	H_3	H_4	H_5	H_6	H_7	H_8
Non GB	$Cu_{0.125}Ni_{0.875}$	13.32	7.95	7.20	8.32	5.73	5.42	5.13	2.74
	$Cu_{0.25}Ni_{0.75}$	13.39	8.23	7.47	8.60	6.06	5.63	5.49	3.10
	$Cu_{0.375}Ni_{0.625}$	14.48	10.09	9.31	10.55	8.27	7.02	7.76	5.20
	$Cu_{0.50}Ni_{0.50}$	13.92	9.30	8.53	9.73	7.34	6.43	6.81	4.36
	$Cu_{0.625}Ni_{0.375}$	14.48	10.07	9.30	10.54	8.25	7.00	7.73	5.17
GB 5	$Cu_{0.125}Ni_{0.875}$	13.02	8.89	8.18	9.30	6.92	6.17	6.68	4.40
	$Cu_{0.25}Ni_{0.75}$	13.10	9.10	8.40	9.52	7.18	6.33	6.98	4.69
	$Cu_{0.375}Ni_{0.625}$	14.02	11.03	10.37	11.54	9.54	7.81	9.75	7.28
	$Cu_{0.50}Ni_{0.50}$	13.53	10.18	9.50	10.65	8.50	7.16	8.54	6.19
	$Cu_{0.625}Ni_{0.375}$	14.02	11.02	10.36	11.52	9.52	7.80	9.73	7.25
GB 13	$Cu_{0.125}Ni_{0.875}$	13.89	7.29	6.51	7.63	4.91	4.90	4.09	1.59
	$Cu_{0.25}Ni_{0.75}$	13.94	7.58	6.79	7.93	5.24	5.11	4.41	1.91
	$Cu_{0.375}Ni_{0.625}$	14.10	8.03	7.23	8.40	5.77	5.44	4.92	2.41
	$Cu_{0.50}Ni_{0.50}$	14.41	8.60	7.79	9.00	6.44	5.87	5.56	3.02
	$Cu_{0.625}Ni_{0.375}$	14.91	9.26	8.43	9.69	7.21	6.35	6.26	3.64

yielding the highest hardness due to the combined effects of solid solution strengthening and grain boundary strengthening. These findings highlight that strategic grain boundary engineering particularly using high-angle boundaries like Σ13 can effectively improve the hardness and mechanical robustness of CuNi alloys. This optimization is especially valuable for applications requiring high wear resistance, dimensional stability, and durability under mechanical loading.

3.4 Effect of alloy compositions and GB on anisotropy factor

Elastic anisotropy is a fundamental property that describes the variation of a material's elastic response with crystallographic direction. It plays a critical role in determining the mechanical performance of crystalline solids, influencing properties such as deformation behavior, crack propagation, and thermal stability. Quantifying anisotropy through various indices enables a deeper understanding of the interplay between atomic arrangement, grain boundaries, and composition. In the present study, the anisotropic behavior of CuNi binary alloys was evaluated using the Universal Anisotropy Index (A^U), shear anisotropy factor (A^G), bulk anisotropy factor (A^B), equivalent Zener anisotropy factor (A^{eq}), log-Euclidean anisotropy index (A^L), and directional shear anisotropy factors (A_1, A_2, A_3), as listed in Table 4.

The Universal Anisotropy Index (A^U) values range from 0.115 to 1.87, depending on composition and grain boundary type. $A^U = 0$ corresponds to a perfectly isotropic solid, while any non-zero value indicates anisotropy.[63] All studied CuNi configurations exhibit elastic anisotropy, with the highest value observed in the Non-GB structure at low Cu content *i.e.*, the structure contains 12.5% of Cu and the lowest in GB Σ13 alloys that contains 62.5% of Cu ($A^U \approx 0.115$). The values of A^G and A^B range from 0 to 1, where 0 indicates perfect isotropy and 1 indicates complete anisotropy.[63] For the studied alloys, A^G values lie between 0.011 and 0.158, indicating measurable shear anisotropy, while A^B values remain at 0.000 across all cases, showing near-isotropic bulk behavior. The cubic shear anisotropy factor ($A_1 = A_2 = A_3$) is constant within each composition and provides a single measure of shear stiffness variation between crystallographic planes in cubic crystals. In Non-GB alloys, A_1 values are higher, reflecting greater anisotropy, whereas GB Σ13 alloys show much lower values approximately 0.686, indicating more uniform shear response due to GB-induced lattice rearrangement. The log-Euclidean anisotropy index (A^L) varies from 0.26 in the most isotropic Non-GB case to 5.97 in the most anisotropic GB Σ13 case. Generally, A^L values lies between 0 and 10.27 for highly anisotropic materials.[63] The equivalent Zener anisotropy factor (A^{eq}) reinforces the anisotropic behaviour for all structures, highlighting the strong dependence of elastic response on both alloy composition and grain boundary character. Higher A^{eq} values in Non-GB structures indicate pronounced directional differences in shear stiffness, while the significantly lower values in GB Σ13 alloys suggest that certain GB types promote a more isotropic elastic environment by disrupting long-range lattice order and homogenizing the bonding network.

Fig. 8 and 9 illustrate the three-dimensional spatial dependence of the bulk modulus (B), Young's modulus (E), shear modulus (G), Vickers hardness (H), and Poisson's ratio (ν) for $Cu_{0.125}Ni_{0.875}$ and $Cu_{0.625}Ni_{0.375}$ respectively in Non-GB, GB Σ5, and GB Σ13 configurations, obtained from the elastic stiffness tensor using MATLAB code.[64] The radial distance from the origin and the color scale represents the magnitude of each property in different crystallographic orientations, allowing direct visualization of elastic anisotropy. For the bulk modulus (B), the surfaces are nearly spherical in all configurations, indicating weak anisotropy in compressibility. Minor distortions appear for GB Σ5 and are more evident for GB Σ13, suggesting that grain boundary misorientation introduces slight directional variation in volumetric stiffness. In both compositions, the difference between maximum and minimum B values remains small, confirming the largely isotropic nature of bulk compression. The Young's modulus (E) shows pronounced anisotropy, with lobe-like maxima and minima. For $Cu_{0.125}Ni_{0.875}$ (Non-GB), the highest stiffness ($\sim E_{max}$) is

Table 4 Influence of alloy compositions and grain boundary on the direction dependent properties of $Cu_xNi_{(1-x)}$ binary alloy

Grain boundary	Grain boundary (GB)	C_{44}^R	C_{44}^V	A^U	A^{eq}	$A_1 = A_2 = A_3$	A^G	A^B	A^L
Non GB	$Cu_{0.125}Ni_{0.875}$	13.69	15.39	1.87	3.25	3.254	0.158	0.000	0.26
	$Cu_{0.25}Ni_{0.75}$	14.29	15.58	1.817	3.20	3.202	0.154	0.000	0.19
	$Cu_{0.375}Ni_{0.625}$	18.47	15.50	1.399	2.81	2.810	0.123	0.000	0.39
	$Cu_{0.50}Ni_{0.50}$	16.73	15.34	1.528	2.93	2.933	0.133	0.000	0.19
	$Cu_{0.625}Ni_{0.375}$	18.42	15.55	0.000	2.81	2.817	0.123	0.000	0.38
GB 5	$Cu_{0.125}Ni_{0.875}$	16.94	9.33	0.918	2.34	2.337	0.084	0.000	1.33
	$Cu_{0.25}Ni_{0.75}$	17.33	9.96	0.958	2.38	2.377	0.087	0.000	1.24
	$Cu_{0.375}Ni_{0.625}$	21.83	9.70	0.741	2.15	2.153	0.069	0.000	1.81
	$Cu_{0.50}Ni_{0.50}$	19.87	9.65	0.809	2.22	2.225	0.075	0.000	1.62
	$Cu_{0.625}Ni_{0.375}$	21.82	9.53	0.728	2.14	2.139	0.068	0.000	1.85
GB 13	$Cu_{0.125}Ni_{0.875}$	14.45	1.60	0.185	1.48	0.677	0.018	0.000	4.92
	$Cu_{0.25}Ni_{0.75}$	15.08	1.56	0.173	1.46	0.686	0.017	0.000	5.07
	$Cu_{0.375}Ni_{0.625}$	16.08	1.50	0.155	1.43	0.699	0.015	0.000	5.31
	$Cu_{0.50}Ni_{0.50}$	17.38	1.32	0.126	1.38	0.724	0.012	0.000	5.77
	$Cu_{0.625}Ni_{0.375}$	18.83	1.30	0.115	1.36	0.734	0.011	0.000	5.97

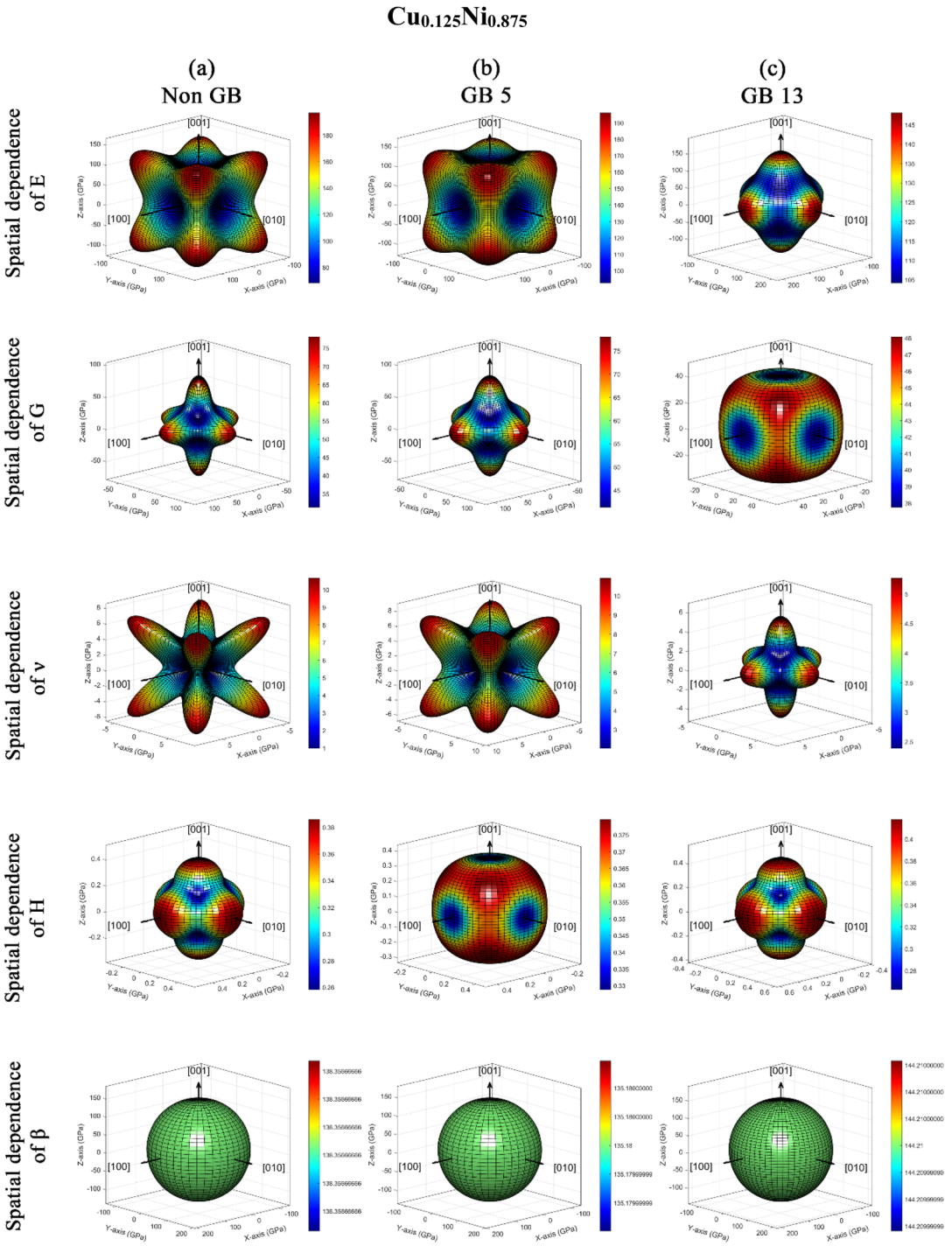

Fig. 8 Spatial dependence of bulk modulus (B), Young's modulus (E), shear modulus (G), hardness (H), and Poisson's ratio (ν) for $Cu_{0.125}Ni_{0.875}$ alloys in (a) Non-GB, (b) GB Σ5, and (c) GB Σ13 configurations.

observed along [111] and intermediate orientations between [111] and [110], while the lowest stiffness ($\sim E_{min}$) occurs along [100]. The introduction of GB Σ5 slightly reduces E_{max} and broadens low-stiffness regions, whereas GB Σ13 significantly distorts the surface, shifting maxima toward off-axis directions. In $Cu_{0.625}Ni_{0.375}$, the lobes are sharper and E_{max} values are higher, with maxima concentrated near [111] and [110], indicating stronger direction-dependent resistance to deformation. The shear modulus (G) distributions also show strong anisotropy, with multi-lobed surfaces reflecting the material's varying resistance to shear deformation. GB Σ13 increases directional variation more noticeably than Σ5, suggesting that the more complex grain boundary structure influences preferred slip systems. The Cu-rich alloy generally maintains higher G values in specific orientations, implying greater shear resistance in those directions. For Vickers hardness (H), the patterns closely

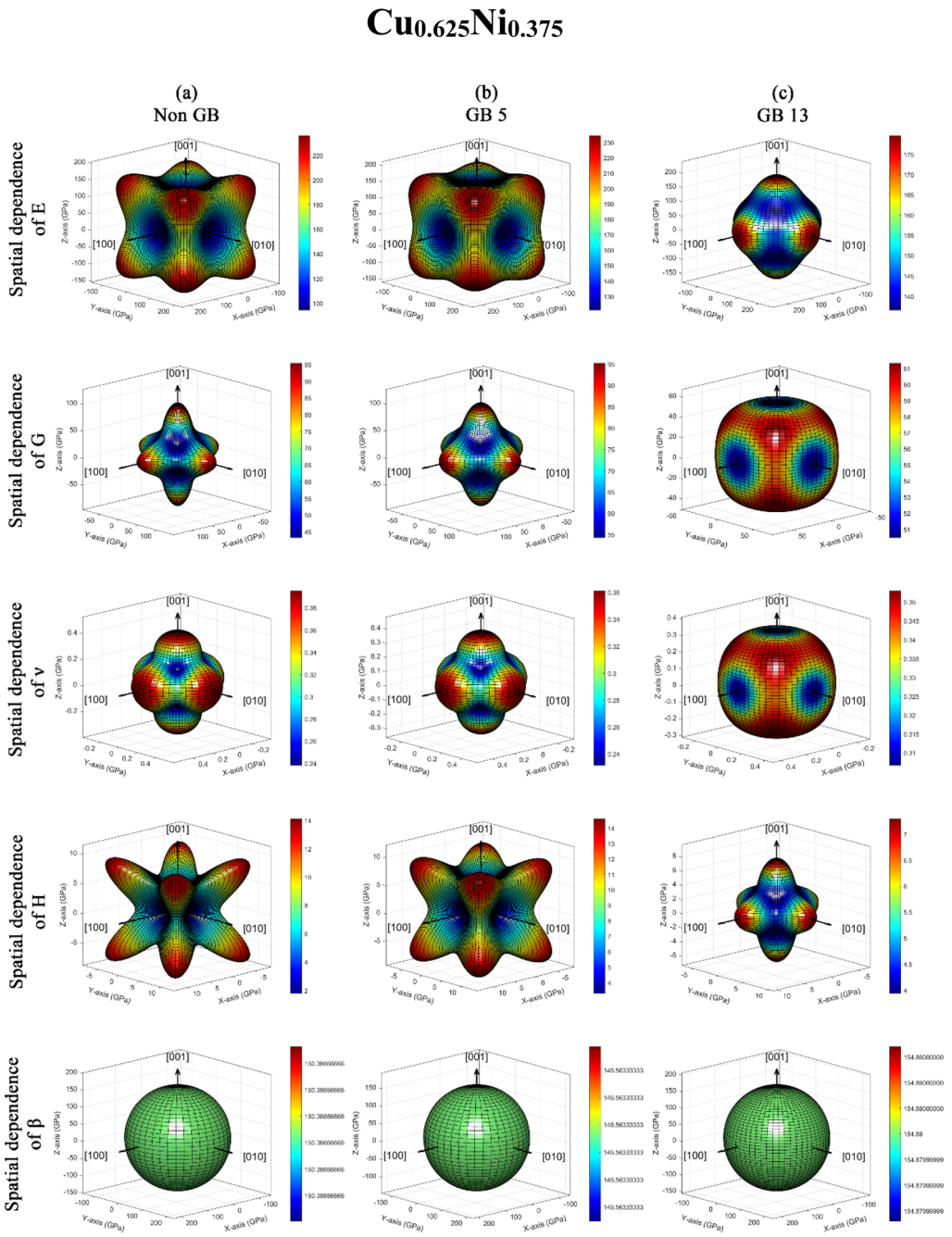

Fig. 9 Spatial dependence of bulk modulus (*B*), Young's modulus (*E*), shear modulus (*G*), hardness (*H*), and Poisson's ratio (ν) for $Cu_{0.625}Ni_{0.375}$ alloys in (a) Non-GB, (b) GB $\Sigma 5$, and (c) GB $\Sigma 13$ configurations.

follow the trends of *G*, as shear resistance is a dominant contributor to indentation hardness. Non-GB structures exhibit more symmetric hardness distributions, while GB-containing structures display more irregular shapes, with $\Sigma 13$ introducing larger contrast between hard and soft orientations. The Cu-rich alloy shows higher hardness peaks, indicating improved resistance to plastic deformation in favorable directions. The Poisson's ratio (ν) distributions show moderate to strong anisotropy. For Non-GB $Cu_{0.125}Ni_{0.875}$, ν_{max} the highest lateral strain occurs along [100], while ν_{min} appears along [111]. GB $\Sigma 13$ broadens ν variation, with maxima shifting toward off-axis orientations between [100] and [110]. In $Cu_{0.625}Ni_{0.375}$, ν ranges are wider, with maxima along [100] and minima near [111], indicating greater heterogeneity in lateral deformation response. Overall, the results reveal that while *B* remains largely isotropic, *E*, *G*, *H*, and ν exhibit strong directionality that is significantly influenced by both grain boundary structure and alloy composition. GB $\Sigma 13$ generally enhances anisotropy, and higher Cu content sharpens directional property contrasts, leading to improved stiffness, shear resistance, and hardness in mechanically favorable orientations.

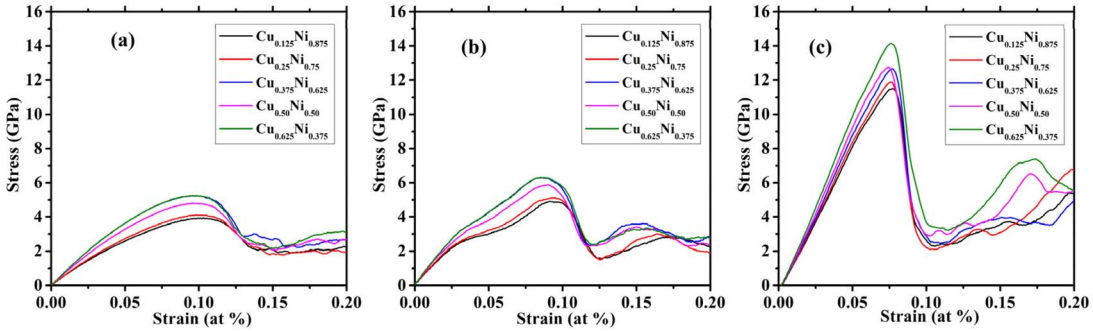

Fig. 10 Stress–strain curve for $Cu_xNi_{(1-x)}$ binary alloy with varying compositions of Cu and Ni and grain boundaries (a) Non-GB, (b) GB Σ5 and (c) GB Σ13.

3.5 Stress–strain curve

Fig. 10 presents the stress–strain response of CuNi binary alloys for different grain boundary configurations: Non-GB, GB Σ5, and GB Σ13. Across all alloy compositions, the GB Σ13 models exhibit the highest peak stress values, indicating superior resistance to dislocation motion and a stronger strengthening effect. This is primarily because high-angle grain boundaries, *i.e.*, GB Σ13, generate greater lattice distortion and act as strong barriers to dislocation transmission, forcing dislocations to pile up and increasing the stress required for plastic yielding.[65] The sharper peaks in GB Σ13 curves reflect this strain accumulation before yielding occurs. GB Σ5 models show intermediate peak stresses, implying moderate obstruction to dislocation glide and a more gradual onset of plastic deformation. In contrast, Non-GB models consistently produce the lowest peak stress and smoother curves, as dislocations move with fewer obstacles. To further understand the microscopic origins of these behaviors, Fig. 11 illustrates the evolution of the atomic structure at three key deformation stages: pre-yield, yielding and post-yield for the Non GB model. Prior to yielding, the structure remains predominantly FCC with only a few isolated distorted atoms, confirming purely elastic behavior. As strain approaches the yield point, dislocation extraction analysis (DXA) reveals the first appearance of partial dislocations and clusters of Non-FCC atoms, indicating the onset of plasticity. After yielding, the number of distorted atoms increases rapidly, accompanied by the formation of continuous dislocation pathways and complex dislocation interactions, which dominate the plastic-flow regime. These observations closely match the mechanical response in Fig. 10 and confirm that yielding is controlled by the nucleation and propagation of dislocations. A similar trend is observed for the GB models, with GB Σ5 showing earlier defect nucleation and GB Σ13 exhibiting delayed dislocation activity. This delay in GB Σ13 correlates directly with its higher peak stress and superior strengthening effect compared to other cases.

The influence of alloy composition is also evident, with increasing Cu content generally leading to higher peak stresses. This trend can be attributed to solid solution strengthening, where size and electronic mismatches between Cu and Ni atoms increase lattice friction stress, hindering dislocation movement through stress field.[66] In some compositions, particularly those with balanced CuNi ratios, the combined effects of solid solution strengthening and grain boundary strengthening are maximized, producing the highest peak stresses. After reaching the peak, all configurations display strain softening, where stress decreases with continued deformation, although the rate and extent of softening vary with both GB type and composition. Therefore, the results highlight that incorporating GB Σ13, along with optimizing alloy composition, can significantly enhance the load-bearing capacity, yield strength, and mechanical toughness of CuNi alloys.

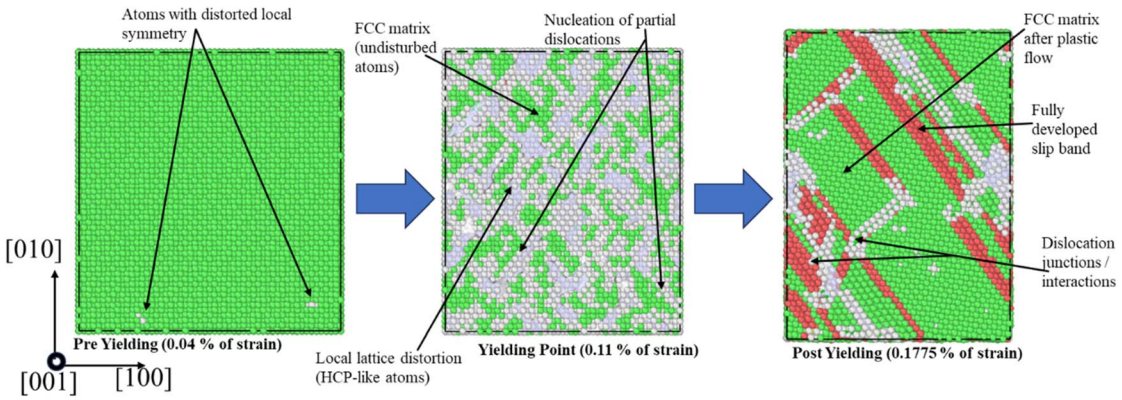

Fig. 11 Pre-yield, yield, and post-yield microstructural evolution of CuNi alloy for Non GB configuration showing dislocation nucleation, slip-band formation using dislocation extraction analysis (DXA).

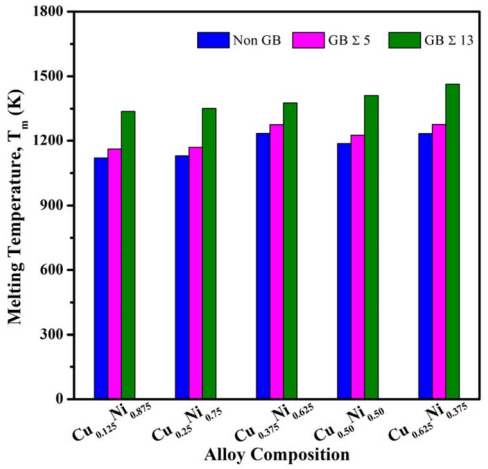

Fig. 12 Influence of alloy compositions and grain boundary on the melting points of CuNi binary alloy.

3.6 Thermophysical analysis of melting points

The melting point is a fundamental thermophysical property representing the temperature at which a material transitions from a solid to a liquid state. It reflects the strength of atomic bonding within the crystal lattice and is directly related to thermal and mechanical stability. In crystalline solids, the melting point is also linked to the Debye temperature (Θ_D), as both are proportional indicators of lattice stiffness and vibrational energy. For cubic systems, the melting temperature (T_m) can be estimated from elastic constants (C_{ij}) using the relation[67]

$$T_m = 354 + \frac{4.5(2C_{11} + C_{33})}{3}$$

Fig. 12 shows the effect of alloy composition and grain boundary on the melting points of CuNi alloys and Table 5 represents the calculted values. Across all compositions, GB containing models exhibit higher melting temperatures than Non GB models, indicating improved thermal stability. GB Σ13 consistently produces the highest T_m values, followed by GB Σ5, with Non GB structures showing the lowest values. This trend can be attributed to the higher atomic disorder at GB Σ13, which increase lattice resistance to thermal vibrations before melting occurs.

Composition also influences the melting point. Increasing Cu content generally raises T_m, reflecting stronger atomic bonding in Cu-rich alloys. Interestingly, for Non GB and GB Σ5 structures, interchanging Cu and Ni concentrations results in similar melting points, suggesting a symmetric solid solution effect, consistent with the trends observed for elastic constants, moduli, and other mechanical properties. In contrast, GB Σ13 shows greater sensitivity to composition changes, with certain intermediate CuNi ratios producing the highest melting temperatures due to an optimal combination of solid solution strengthening and GB-induced lattice stabilization.

Table 5 Influence of grain boundary on melting temperature of $Cu_xNi_{(1-x)}$ Binary alloy

	Grain Boundary		
Alloy Composition	Non GB	GB Σ5	GB Σ13
$Cu_{0.125}Ni_{0.875}$	1120.665	1162.56	1337.385
$Cu_{0.25}Ni_{0.75}$	1130.745	1169.58	1351.74
$Cu_{0.375}Ni_{0.625}$	1234.38	1275.78	1377.075
$Cu_{0.50}Ni_{0.50}$	1186.635	1225.92	1411.77
$Cu_{0.625}Ni_{0.375}$	1234.02	1276.275	1463.43

4. Conclusion

The present work demonstrates how grain boundary structure and alloy composition collectively govern the mechanical, elastic, and thermal behavior of CuNi binary alloys at the atomic scale. Molecular dynamics simulations revealed that the GB Σ13 (314) configuration provides the highest combination of stiffness, hardness, melting point, and peak tensile strength, particularly as Cu content increases. This strengthening is achieved while maintaining ductility, as confirmed by Pugh's ratio above 2.7, Poisson's ratio of about 0.34, Cauchy pressure values exceeding 60 GPa, and compliance with Frantsevich's criterion in GB Σ13. Across all configurations, Young's modulus remains the dominant modulus and GB Σ5 (310) exhibits the highest elastic moduli overall, with values approaching 181.49 GPa for $Cu_{0.625}Ni_{0.375}$ for GB Σ5, reflecting strong resistance to uniaxial tensile deformation. Further, In GB Σ13, the $Cu_{0.125}Ni_{0.875}$ composition shows the highest $\mu_M = 3.82$, indicating superior machinability compared to other compositions and configurations. Anisotropy analysis indicates non-uniform directional mechanical properties across GB types. Beyond confirming established FCC alloy trends, these findings highlight practical pathways for tailoring GB characteristics to meet specific performance requirements. The ability of GB Σ13 to sustain higher peak stresses especially with increased Cu content stresses and hardness greater than GB Non, offers a strategic advantage in applications subjected to high mechanical loads or elevated temperatures. Thermal stability analysis further indicates that GB Σ13 with the $Cu_{0.625}Ni_{0.375}$ composition exhibits the highest melting point among all configurations, making it the most suitable for elevated-temperature service. Likewise, the minimal performance change upon reversing Cu and Ni ratios in Non-GB and GB Σ5 suggests potential cost savings in alloy fabrication through relaxed composition tolerances. Such insights are directly relevant to the design of high-strength, corrosion-resistant materials for marine hardware, cryogenic systems, and heat-exchange components. By linking atomic-scale GB behavior to macroscopic performance targets, this study provides a foundation for precision engineering of CuNi alloys in demanding structural environments.

Conflicts of interest

There are no conflicts of interest to declare.

Data availability

The data sets generated and/or analyzed in this study are available from the corresponding author on reasonable request.

Acknowledgements

The authors are grateful to the Pabna University of Science and Technology, Bangladesh for financial support during this research work.

References

1 A. R. Bailey, Binary Alloying, in *A Text-Book of Metallurgy*, ed. A. R. Bailey, Macmillan Education UK, London, 1960, pp. 31–48.
2 D. V. Louzguine, H. Kato, L. V. Louzguina and A. Inoue, High-strength binary Ti–Fe bulk alloys with enhanced ductility, *J. Mater. Res.*, 2004, **19**, 3600.
3 J. Zhang, C. Wang, A. Hou, J. Wu, D. Lian, M. Zhang and Z. Yu, Improvement of Corrosion and Wear Resistance of Mg-Li Alloy by Binary- and Ternary-Layered Double Hydroxide/Steam Coating Composite Coatings, *J. Mater. Eng. Perform.*, 2025, **34**, 7083.
4 G. M. Scamans, N. Birbilis, and R. G. Buchheit, 3.08 – Corrosion of Aluminum and Its Alloys, in *Shreir's Corrosion*, ed. B. Cottis, M. Graham, R. Lindsay, S. Lyon, T. Richardson, D. Scantlebury, and H. Stott, Elsevier, Oxford, 2010, pp. 1974–2010.
5 S. A. Batool, A. Ahmad, A. Wadood, A. Mateen and W. Hussain, Development of Lightweight Aluminum-Titanium Alloys for Aerospace Applications, *Key Eng. Mater.*, 2018, **778**, 22.
6 Q. Jiang, D. Lu, N. Wang, X. Wang, J. Zhang, J. Duan and B. Hou, The corrosion behavior of Mg–Nd binary alloys in the harsh marine environment, *J. Magnesium Alloys*, 2021, **9**, 292.
7 R. Xie, Q. Jiang, C. Liu, X. Wu, Y. Geng, J. Duan and B. Hou, The microstructure and corrosion characteristic of Al-10 wt%RE (Re= Ce, Nd, La, Y) binary aluminum alloys in natural seawater, *J. Mater. Res. Technol.*, 2024, **33**, 6408.
8 Z. Tang, J. Niu, H. Huang, H. Zhang, J. Pei, J. Ou and G. Yuan, Potential biodegradable Zn-Cu binary alloys developed for cardiovascular implant applications, *J. Mech. Behav. Biomed. Mater.*, 2017, **72**, 182.
9 M.-X. Wang, H. Zhu, G.-J. Yang, K. Liu, J.-F. Li and L.-T. Kong, Solid-solution strengthening effects in binary Ni-based alloys evaluated by high-throughput calculations, *Mater. Des.*, 2021, **198**, 109359.
10 K. Osamura, H. Okuda, S. Ochiai, M. Takashima, K. Asano, M. Furusaka, K. Kishida and F. Kurosawa, Precipitation Hardening in Fe-Cu Binary and Quaternary Alloys, *ISIJ Int.*, 1994, **34**, 359.
11 I. H. Kim, H. S. Oh, S. J. Kim and E. S. Park, Rapid assessment of solid solution hardening via atomic size misfit parameter in refractory concentrated alloys, *J. Alloys Compd.*, 2021, **886**, 161320.
12 G. Ge, F. Chen, X. Tang, C. Li, J. Gao, S. Li and Z. Geng, Effects of order and disorder on the defect evolution of NiFe binary alloys from atomistic simulations, *Nucl. Instrum. Methods Phys. Res., Sect. B*, 2021, **498**, 27.
13 D. S. Aidhy, Chemical randomness, lattice distortion and the wide distributions in the atomic level properties in high entropy alloys, *Comput. Mater. Sci.*, 2024, **237**, 112912.
14 F. L. Williams and D. Nason, Binary alloy surface compositions from bulk alloy thermodynamic data, *Surf. Sci.*, 1974, **45**, 377.
15 W. Weißbach, *Werkstoffkunde und Werkstoffprüfung*, Springer-Verlag, 2013.
16 J. B. Morake, J. M. Mutua, M. M. Ruthandi, E. O. Olakanmi and A. Botes, Failure analysis of corroded heat exchanger CuNi tubes from a geothermal plant, *Eng. Failure Anal.*, 2023, **153**, 107543.
17 P. Sakiewicz, R. Nowosielski and R. Babilas, Production aspects of inhomogeneous hot deformation in as-cast CuNi25 alloy, *Indian J. Eng. Mater. Sci.*, 2015, **22**, 389.
18 S. Manzoor, T. Munawar, S. Gouadria, M. Sadaqat, A. G. Abid, A. Munawar, F. Hussain, F. Iqbal, I. Ahmad and M. N. Ashiq, Nanopetals shaped CuNi alloy with defects abundant active surface for efficient electrocatalytic oxygen evolution reaction and high performance supercapacitor applications, *J. Electrochem. Energy Convers. Storage*, 2022, **55**, 105488.
19 J. Ahmed, K. V. Ramanujachary, S. E. Lofland, A. Furiato, G. Gupta, S. M. Shivaprasad and A. K. Ganguli, Bimetallic Cu–Ni nanoparticles of varying composition (CuNi3, CuNi, Cu3Ni), *Colloids Surf., A*, 2008, **331**, 206.
20 R. Devi Janani, S. A. Salman, K. Pavithra Priyadharshini and V. Karthik, Effect of composition on the stacking fault energy of copper-nickel alloys using molecular dynamics simulations, *Mater. Today: Proc.*, 2021, **39**, 1796.
21 L. Xu, Z. Huang, Q. Shen and F. Chen, Effect of stacking fault energy on hetero-deformation in gradient nanograined Cu-Ni alloys, *Mech. Mater.*, 2024, **196**, 105074.
22 M. M. Rahman, Md. S. Islam and N. Anjum, Investigation on mechanical behaviors of Cu-Ni binary alloy nanopillars: a molecular dynamics study, *J. Mol. Model.*, 2020, **26**, 214.
23 J. Teeriniemi, P. Taskinen and K. Laasonen, First-principles investigation of the Cu–Ni, Cu–Pd, and Ni–Pd binary alloy systems, *Intermetallics*, 2015, **57**, 41.
24 R. Duran, P. Stender, S. M. Eich and G. Schmitz, Atom probe study of the miscibility gap in CuNi thin films and microstructure development, *Microsc. Microanal.*, 2022, **28**, 1359.
25 M. Chen, The Optimum Grain Size of Nanocrystalline CuNi Alloy with Grain Boundary Segregation Structure, *Cryst. Growth Des.*, 2024, **24**, 262.
26 G. Tréglia, B. Legrand and P. Maugain, Surface segregation in CuNi and AgNi alloys formulated as an area-preserving map, *Surf. Sci.*, 1990, **225**, 319.
27 C. Fu, J. Yan, J. Yu, Y. Ren and S. Li, Evaluating Binary Molybdenum Alloys as Strong and Ductile High-Temperature Materials, *Materials*, 2025, **18**, 14.

28 L. Z. Mohamed, O. A. E. Kady, M. M. Lotfy, H. A. Ahmed and F. A. Elrefaie, Characteristics of Ni- Cr Binary Alloys Produced by Conventional Powder Metallurgy, *Key Eng. Mater.*, 2020, **835**, 214.

29 P. E. L'vov and V. V. Svetukhin, Influence of grain boundaries on the distribution of components in binary alloys, *Phys. Solid State*, 2017, **59**, 2453.

30 M. A. Gibson and C. A. Schuh, Segregation-induced changes in grain boundary cohesion and embrittlement in binary alloys, *Acta Mater.*, 2015, **95**, 145.

31 M. Hillert and B. Sundman, A treatment of the solute drag on moving grain boundaries and phase interfaces in binary alloys, *Acta Metall.*, 1976, **24**, 731.

32 M. S. Daw and M. I. Baskes, Embedded-atom method: Derivation and application to impurities, surfaces, and other defects in metals, *Phys. Rev. B:Condens. Matter Mater. Phys.*, 1984, **29**, 6443.

33 S. M. Foiles, M. I. Baskes and M. S. Daw, Embedded-atom-method functions for the fcc metals Cu, Ag, Au, Ni, Pd, Pt, and their alloys, *Phys. Rev. B:Condens. Matter Mater. Phys.*, 1986, **33**, 7983.

34 R. A. Johnson, Alloy models with the embedded-atom method, *Phys. Rev. B:Condens. Matter Mater. Phys.*, 1989, **39**, 12554.

35 Y. Mishin, D. Farkas, M. J. Mehl and D. A. Papaconstantopoulos, Interatomic potentials for monoatomic metals from experimental data and ab initio calculations, *Phys. Rev. B:Condens. Matter Mater. Phys.*, 1999, **59**, 3393.

36 W. Kohn and L. J. Sham, Self-Consistent Equations Including Exchange and Correlation Effects, *Phys. Rev.*, 1965, **140**, A1133.

37 F. Ercolessi, M. Parrinello and E. Tosatti, Simulation of gold in the glue model, *Philos. Mag. A*, 1988, **58**, 213.

38 F. Fischer, G. Schmitz and S. M. Eich, A systematic study of grain boundary segregation and grain boundary formation energy using a new copper–nickel embedded-atom potential, *Acta Mater.*, 2019, **176**, 220.

39 M. S. Daw and M. I. Baskes, Semiempirical, Quantum Mechanical Calculation of Hydrogen Embrittlement in Metals, *Phys. Rev. Lett.*, 1983, **50**, 1285.

40 A. P. Thompson, H. M. Aktulga, R. Berger, D. S. Bolintineanu, W. M. Brown, P. S. Crozier, P. J. In't Veld, A. Kohlmeyer, S. G. Moore and T. D. Nguyen, LAMMPS-a flexible simulation tool for particle-based materials modeling at the atomic, meso, and continuum scales, *Comput. Phys. Commun.*, 2022, **271**, 108171.

41 P. Hirel, Atomsk: A tool for manipulating and converting atomic data files, *Comput. Phys. Commun.*, 2015, **197**, 212.

42 R. Freitas, R. E. Rudd, M. Asta and T. Frolov, Free energy of grain boundary phases: Atomistic calculations for $Σ$5(310)[001] grain boundary in Cu, *Phys. Rev. Mater.*, 2018, **2**, 093603.

43 M. Shamsuzzoha, I. Vazquez, P. A. Deymier and D. J. Smith, The atomic structure of a Σ=5[001]/(310) grain-boundary in an Al-5% Mg alloy by high-resolution electron microscopy, *Interface Sci.*, 1996, **3**, 227.

44 V. S. Boyko and A. M. Levine, The atomic structure of large-angle grain boundaries $Σ5$ and $Σ13$ in ${\rm YBa_2Cu_3O_{7-δ}}$ and their transport properties, *Phys. Rev. B:Condens. Matter Mater. Phys.*, 2001, **64**, 224525.

45 A. Stukowski, Visualization and analysis of atomistic simulation data with OVITO–the Open Visualization Tool, *Modell. Simul. Mater. Sci. Eng.*, 2009, **18**, 015012.

46 A. Stukowski and K. Albe, Extracting dislocations and non-dislocation crystal defects from atomistic simulation data, *Modell. Simul. Mater. Sci. Eng.*, 2010, **18**, 085001.

47 H. Tsuzuki, P. S. Branicio and J. P. Rino, Structural characterization of deformed crystals by analysis of common atomic neighborhood, *Comput. Phys. Commun.*, 2007, **177**, 518.

48 W. Voigt, A determination of the elastic constants for beta-quartz lehrbuch de kristallphysik, *Teubner Leipzig.*, 1928, **40**, 2856.

49 A. Reuss, Calculation of the flow limits of mixed crystals on the basis of the plasticity of monocrystals, *Z. Angew. Math. Mech.*, 1929, **9**, 49.

50 R. Hill, The elastic behaviour of a crystalline aggregate, *Proc. Phys. Soc., London, Sect. A*, 1952, **65**, 349.

51 Y. Liu, W.-C. Hu, D. Li, X.-Q. Zeng, C.-S. Xu and X.-J. Yang, First-principles investigation of structural and electronic properties of MgCu2 Laves phase under pressure, *Intermetallics*, 2012, **31**, 257.

52 M. Born, On the Stability of Crystal Lattices. I, in *Mathematical Proceedings of the Cambridge Philosophical Society*, Cambridge University Press, 1940, vol. 36, pp. 160–172.

53 Y. Wei, B. Niu, Q. Liu, Z. Liu and C. Jiang, First-Principles Calculations of Structural and Mechanical Properties of Cu–Ni Alloys, *Crystals*, 2023, **13**, 43.

54 S. F. Pugh, XCII. Relations between the elastic moduli and the plastic properties of polycrystalline pure metals, *London, Edinburgh Dublin Phil. Mag. J. Sci.*, 1954, **45**, 823.

55 J. J. Lewandowski, W. H. Wang and A. L. Greer, Intrinsic plasticity or brittleness of metallic glasses, *Philos. Mag. Lett.*, 2005, **85**, 77.

56 M. H. Kabir, M. M. Hossain, M. A. Ali, M. M. Uddin, M. L. Ali, M. Z. Hasan, A. A. Islam and S. H. Naqib, First principles study of mechanical, thermal, electronic, optical and superconducting properties of C40-type germanide-based MGe2 (M= V, Nb and Ta), *Results Phys.*, 2023, **51**, 106701.

57 M. Roknuzzaman, K. Ostrikov, H. Wang, A. Du and T. Tesfamichael, Towards lead-free perovskite photovoltaics and optoelectronics by ab-initio simulations, *Sci. Rep.*, 2017, **7**, 14025.

58 I. N. Frantsevich, F. F. Voronov, and S. A. Bakuta, *Elastic Constants and Elastic Moduli of Metals and nonmetals(In Russian)*, Kiev, Izdatel'stvo Naukova Dumka, 1982, 288.

59 Z. Sun, D. Music, R. Ahuja and J. M. Schneider, Theoretical investigation of the bonding and elastic properties of nanolayered ternary nitrides, *Phys. Rev. B:Condens. Matter Mater. Phys.*, 2005, **71**, 193402.

60 X.-Q. Chen, H. Niu, D. Li and Y. Li, Modeling hardness of polycrystalline materials and bulk metallic glasses, *Intermetallics*, 2011, **19**, 1275.
61 M. I. Naher and S. H. Naqib, Possible applications of Mo2C in the orthorhombic and hexagonal phases explored via ab-initio investigations of elastic, bonding, optoelectronic and thermophysical properties, *Results Phys.*, 2022, **37**, 105505.
62 E. Pellicer, A. Varea, K. M. Sivaraman, S. Pané, S. Suriñach, M. D. Baró, J. Nogués, B. J. Nelson and J. Sort, Grain boundary segregation and interdiffusion effects in nickel-copper alloys: an effective means to improve the thermal stability of nanocrystalline nickel, *ACS Appl. Mater. Interfaces*, 2011, **3**, 2265.
63 S. I. Ranganathan and M. Ostoja-Starzewski, Universal Elastic Anisotropy Index, *Phys. Rev. Lett.*, 2008, **101**, 055504.
64 M. Liao, *Hitliaomq/ElasticPOST: ElasticPOST*, 2019.
65 H. Pan, Y. He and X. Zhang, Interactions between Dislocations and Boundaries during Deformation, *Materials*, 2021, **14**, 1012.
66 H. A. Roth, C. L. Davis and R. C. Thomson, Modeling solid solution strengthening in nickel alloys, *Metall. Mater. Trans. A*, 1997, **28**, 1329–1335.
67 M. E. Fine, L. D. Brown and H. L. Marcus, Elastic constants versus melting temperature in metals, *Scr. Metall.*, 1984, **18**, 951.